Nuclear Materials and Energy 41 (2024) 101744

Contents lists available at ScienceDirect

Nuclear Materials and Energy

journal homepage: www.elsevier.com/locate/nme

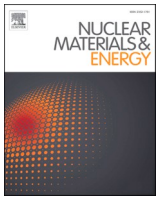

Experimental study on metallic impurity behavior with boronization wall conditioning in EAST tokamak

Yunxin Cheng [a], Ling Zhang [a,*], Ailan Hu [a], Shigeru Morita [b], Wenmin Zhang [a,c], Chengxi Zhou [a], Darío Mitnik [d], Fengling Zhang [a,c], Jiuyang Ma [a,c], Zhengwei Li [a,e], Yiming Cao [a,e], Haiqing Liu [a,*]

[a] Institute of Plasma Physics Chinese Academy of Sciences, Hefei 230031, China
[b] National Institute for Fusion Science, Toki 509-5292, Gifu, Japan
[c] University of Science and Technology of China, Hefei 230026, China
[d] Instituto de Astronomía y Física del Espacio (CONICET-Universidad de Buenos Aires), Buenos Aires 1428, Argentina
[e] Anhui University, Hefei 230601, China

ARTICLE INFO

Keywords:
EAST
Plasma-facing materials
Boronization wall conditioning
Mertallic impurity
EUV spectrometer

ABSTRACT

Operation of EAST tokamak with full metal wall without any wall conditioning are attempted in 2023 and 2024 experimental campaign to address the issues related to ITER tungsten wall operation. It is found that H-mode plasma could be sustained even with a substantial increase in metallic impurity content caused by strong plasma-wall interaction under uncoated metal wall. Boronization wall conditioning is therefore performed to improve the plasma performance with higher injected power. This study aims to quantitatively assess the impact of boronization wall conditioning on metallic impurity concentration and behavior in the EAST tokamak. It is then proved to be an effective wall conditioning approach for significantly controlling high-Z impurity content. In this work, the impurity spectra at extreme ultraviolet (EUV) wavelength range measured by sets of fast-time-response and space-resolved EUV spectrometers are widely used in the data analysis. The variation in the boron content in plasma after boronization are investigated by monitoring the 2nd order of B V line at 48.59 Å. It is found that the persistence time of boron in EAST device after a boronization with 10 g of carborane ($C_2B_{10}H_{12}$) is about 2000 s (~150 shots) of discharge duration. The impact of different wall conditions (uncoated metal wall and boron coated wall) on metallic impurity content are then quantitatively studied. After boronization, the concentration of tungsten (C_W) and molybdenum (C_{Mo}) dropped by 85 %, e. g., from 2.0×10^{-4} to 4.1×10^{-5} and from 4.6×10^{-5} to 6.3×10^{-6}, respectively. While the concentration of copper (C_{Cu}) and iron (C_{Fe}) decreased by approximately 50 % and 65 %, respectively, e. g., from 4.3×10^{-5} to 2.1×10^{-5} and from 2.0×10^{-4} to 6.9×10^{-5}. A comparison of the line emission profiles from tungsten ions of $W^{26+} - W^{32+}$ and W^{43+} before and after boronization reveals an overall reduction in the intensity while without obvious change in the profile shape, which suggests a reduction in metallic impurities source after boronization instead of altering impurity transport in core plasma significantly.

1. Introduction

Plasma facing materials (PFMs) are utterly important in fusion tokamak devices due to inevitable plasma-wall interaction. These PFMs will be exposed to high-energy radiation and particle streams for a long time in tokamaks, especially in future fusion reactors. The tungsten is top candidate PFMs due to good characteristics of high sputtering threshold, high melting point, small retention of tritium and high neutron resistance. Tungsten materials are planned to be used for the divertor and the first wall of ITER in the future. The use of tungsten is also planned for the CFETR [1]. Since 2010 first wall of the EAST has been upgraded to be molybdenum alloy. The original graphite upper and lower divertors of the EAST has been replaced with tungsten mono-blocks or flat tiles since 2014 and 2021 respectively [2,3]. Since 2021, EAST has been operating in a full metal environment. However, tungsten, being a high-Z element, raise challenges by significant radiation

* Corresponding authors.
E-mail addresses: zhangling@ipp.ac.cn (L. Zhang), hqliu@ipp.ac.cn (H. Liu).

https://doi.org/10.1016/j.nme.2024.101744
Received 28 June 2024; Received in revised form 16 September 2024; Accepted 20 September 2024
Available online 21 September 2024

power loss, leading to degraded plasma performance or even discharge termination [4]. How to control the content of tungsten impurity in the plasma is one of key issues for ITER and EAST, as well as for other fusion devices using tungsten plasma-facing components (PFCs), e.g., ASDEX-U [5], WEST [6], JET [7]. Coating on the surface of PFCs with low-Z materials is a practical method to reduce impurity sources and edge particle recycling. The lithium coating has been proven to be extremely effective in reducing particle recycling and H/(H+D) ratio [8]. However, the lithium has a high retention rate for tritium. Siliconization can properly reduce particle recycling, but its effect only lasts for only several shots [8]. Boron has a low retention rate for tritium, and boronization has been proved to be an effective wall conditioning approach to reduce particle recycling and impurity flux in many devices [9–12]. Consequently, boronization with carborane ($C_2B_{10}H_{12}$) by ICRF has been applied to EAST [13]. Moreover, boronization will also be applied in ITER [14]. Large number of high-power long-pulse discharges with metal and boronized wall were executed during EAST last two campaigns in 2023 and 2024 to verify the feasibility of ITER operating scenario.

Investigating impurity behavior under different wall conditions is crucial for evaluating the effect of wall conditioning. Sets of Extreme Ultraviolet (EUV) spectrometer systems have been developed in EAST to observe the time behavior of impurity ions and to measure their spatial distribution from plasma edge to core [15–19]. These impurity-related spectroscopic diagnostics are powerful platform to study high- and low-Z impurity behaviors and transport in plasma. The impact of boronization on the behavior and content of metallic impurity will be quantitatively assessed in this work.

The remainder of this article is organized as follows. The EAST tokamak and impurity-related spectroscopic diagnostics are introduced in Section 2. The influence of boronization on impurity composition and the variation of metallic impurity content after boronization are analyzed in Section 3. Finally, summary and discussion are given in Section 4.

2. Experimental setup

EAST is a full superconducting tokamak device with flexible plasma configurations, e.g., limiter, upper single null (USN), lower single null (LSN), and double null (DN) configurations. Its major radius R=1.85 m, minor radius a = 0.45 m, elongation ratio k = 1.2–2, maximum plasma current I_p = 1 MA, and maximum designed center toroidal field (TF) strength B_t = 3.5 T. In order to achieve steady-state high-performance plasma operation to support ITER operating scenario assessment, recently the EAST heating system has been upgraded to improve current drive and heating capability, including LHCD system (6 MW), ECRH system (3 MW), ICRF system (12 MW), NBI systems (8 MW) [3]. The upper and lower divertor of EAST were upgraded in 2014 and 2021, respectively, by replacing the carbon divertor with tungsten divertor in order to increase the capability of heat and particle exhaust of divertor plate from 2 to 10 MW/m^2. The guard limiter of LHCD antenna and main limiter were replaced by tungsten material in 2018 and 2022, respectively. The first wall at the high field side (HFS) is primarily composed of tiles made by titanium-zirconium-molybdenum (TZM) alloy, while the areas exposed to neutral beam injection (NBI) shines through are composed of graphite tiles. Therefore, since 2021 the EAST has been operating with nearly full metal wall. Besides, the antennas of various radio frequency heating systems are made of copper, and there are numerous stainless-steel components inside the device, which may introduce iron impurity ions into the plasma. As a result, effective control of metal impurities, such as copper, iron, molybdenum, and tungsten, has become a critical challenge for achieving long-pulse, high-performance plasma discharges in the EAST.

In EAST, the control of edge particle recycling and impurity flux is mainly achieved through wall conditioning of lithium coating [20–22], siliconization [23] or boronization [8,13]. Both He ICRF-assisted boronization [24,25] and glow discharge (GDC) [26] boronization have been used for wall conditioning in EAST 2023 and 2024 experimental campaign. Each time of boronization usually consumes 10 g of carborane ($C_2B_{10}H_{12}$). In this study, the experimental results under ICRF-assisted boronization were analyzed. The thickness of the boron film is about 100–200 nm [25], and the film is composed of 51 % boron, 37 % carbon, and 12 % oxygen. Boronization has been demonstrated to effectively suppress impurities [13]. However, boronization also introduces H to the wall, which leads to high wall retention rate and high H/(H+D) ratio. Recently it was found that changing the ICRF-assistant gas from He to D_2 could achieve a lower H/(H+D) ratio after boronization.

Several Extreme Ultraviolet (EUV) spectrometer systems have been installed on the EAST to measure the line emissions from multiple impurity species including low-Z and high-Z impurity ions [15–19]. In this work, a space-resolved EUV spectrometer named 'EUV_Long2_u' is used to investigate the intensity profile of line emissions from impurity ions [15]. A fast-time-response EUV spectrometer with temporal resolution of 5 ms/frame called 'EUV_Long_a' is used to observe the temporal behavior of the impurities in core plasma [16]. Fig. 1 shows the lines of

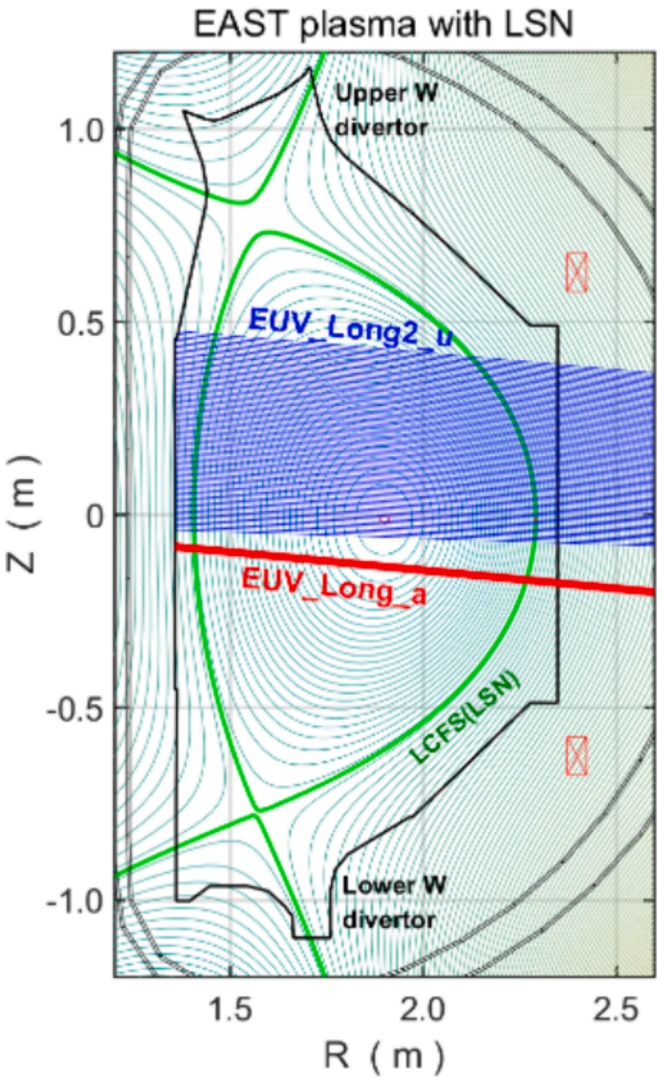

Fig. 1. Poloidal cross section of EAST tokamak (last closed flux surface: thick green line) and lines of sight (LOS) of fast-time-response EUV spectrometer (EUV_Long_a: red line) and space-resolved EUV spectrometer (EUV_Long2_u: blue lines). (For interpretation of the references to color in this figure legend, the reader is referred to the web version of this article.)

sight of these two EUV spectrometers. After absolute intensity calibration, the high-Z impurity concentration and radial density profile of high-Z impurity ions in the core plasma can be obtained [27].

In EAST experiment, the temporal evolution of the electron temperature and line-averaged density are measured by heterodyne radiometer [28] and solid-source interferometer [29], respectively. The electron density profile is measured with polarimeter interferometer system [30]. The radiation power loss is measured by absolute extreme ultraviolet (AXUV) diagnostic system [31].

3. Impurity behavior under metal and boronized wall

3.1. Impurity composition and its time evolution during typical discharges

The temporal evolution of plasma parameters and impurity radiation and line emission intensity in two typical discharges before and first day after boronization are illustrated in Fig. 2. In both discharges, ECRH with power of 3.0 MW and LHW with 1.0 MW are injected, and the toroidal magnetic field, B_t, plasma current, I_p, electron density, n_{e0}, and electron temperature, T_{e0}, are similar, i.e., 2.5 T, 400 kA, 4.0 $\times$ 10^{19} m^{-3}, and 4.0 keV, respectively. Moreover, the electron density and temperature profile of these two shots are also similar in shape, as shown in Fig. 3. Only the flat-top phase of T_{e0} and impurity content are presented due to significant errors at I_p ramp-up and ramp-down phase. It is found that after boronization, the confinement of the plasma slightly improved, and the radiative power at both the plasma edge and core reduced by 85 % and 75 %, respectively. The radiation power contributed by each metallic impurity has been calculated using cooling rate from ADAS database. For the H-mode discharge, tungsten and molybdenum contribute about 60 % and 20 % of the total radiation power, respectively. The fraction of radiation power due to copper and iron impurity is about 10 %. The evaluated relative flux of tungsten atoms, based on the S/XB coefficient [32] and the WI line emission measured by divertor visible spectroscopy [33], suggests a significant reduction in tungsten impurity sources after boronization, as shown in Fig. 2 (f). In terms of the variation of impurity content (Fig. 2 (g)-(l)), the content of oxygen and all metallic impurities decreased with varying degrees during I_p flat-top phase. During the current ramp-up phase, the n_e-normalized line emission intensity of low-Z impurities is quite strong due to the lower electron temperature. As the electron temperature rises, low-Z impurity ions migrate outward, resulting in a gradual decrease in the n_e-normalized line emission intensity of low-Z impurities as shown in Fig. 2 (g) and (h). After boronization, the concentration of iron (C_{Fe}) and copper (C_{Cu}) decreases by 65 %, e. g., from 1.7 $\times$ 10^{-4} to 6.0 $\times$ 10^{-5} and from 4.2 $\times$ 10^{-5} to 1.3 $\times$ 10^{-5}, respectively. While the concentration of tungsten (C_W) and molybdenum (C_{Mo}) is reduced by 85 %, e.g., from 1.8 $\times$ 10^{-4} to 2.8 $\times$ 10^{-5} and from 3.0 $\times$ 10^{-5} to 4.2 $\times$ 10^{-6}, respectively. Here, the concentration of metallic impurities can be evaluated based on the absolute intensity of line emission as shown in Fig. 4, photonic emission coefficients from the ADAS database and fraction abundance from ionization equilibrium [27]. After boronization, the reduction rate of tungsten and molybdenum is significantly greater than that of iron and copper. A detailed comparison will be extended for longer period after boronization in Section 3.2.

EUV spectra at 21–150 Å measured at t = 5.0 s in the two similar discharges before and after boronization are plotted in Fig. 4. Identification of line emissions is based on the results from our previous work [34,35]. Before boronization, the tungsten unresolved transition array (W-UTA) at 45–70 Å composed of W^{26+}-W^{45+} ions with strong intensity could be observed, and line emissions of W^{26+} at 49.0 Å, W^{27+} at 49.403 Å, W^{43+} at 61.334 Å and W^{45+} at 62.336 Å could be easily identified from the W-UTA. Isolated lines from high charge states of tungsten ions appear at long wavelength ranges of 120–140 Å, e.g., W^{43+} at 126.29 Å and W^{45+} at 126.998 Å. Moreover, line emissions from other high-Z metallic impurities of molybdenum, copper and iron could be easily observed with strong intensity, e.g., Mo XXIV-Mo XXXII (Mo^{23+} – Mo^{31+}) at 70–130 Å, Cu XXII-Cu XXVI (Cu^{21+} – Cu^{25+}) at 90–120 Å and Fe XVIII-Fe XXIII (Fe^{17+} – Fe^{22+}) at 90–140 Å. It could be found that after boronization the intensities of W-UTA dramatically decreased, and only line emissions from highly charged (Mg- and Na- like) Mo ion with weak intensity could be observed, i.e., Mo XXXI at 115.999 Å, Mo XXXII 127.868 Å. That from lower charge state Mo ions are difficulty to identify, e.g., for Mo XXIV 70.726 Å, Mo XXVIII 84.78 Å, Mo XXIX 88.173 Å. Line emissions from iron and copper ions also decrease largely but still maintain certain intensity after boronization, e.g., Fe XIV 93.926 Å, Fe XXIII 132.906 Å, Fe XXIII 135.812 Å, Cu XXIII 98.845 Å, Cu XXVI 111.186 Å. The comparison of the spectra suggests that boronization wall conditioning is beneficial on the suppression of all the high-Z

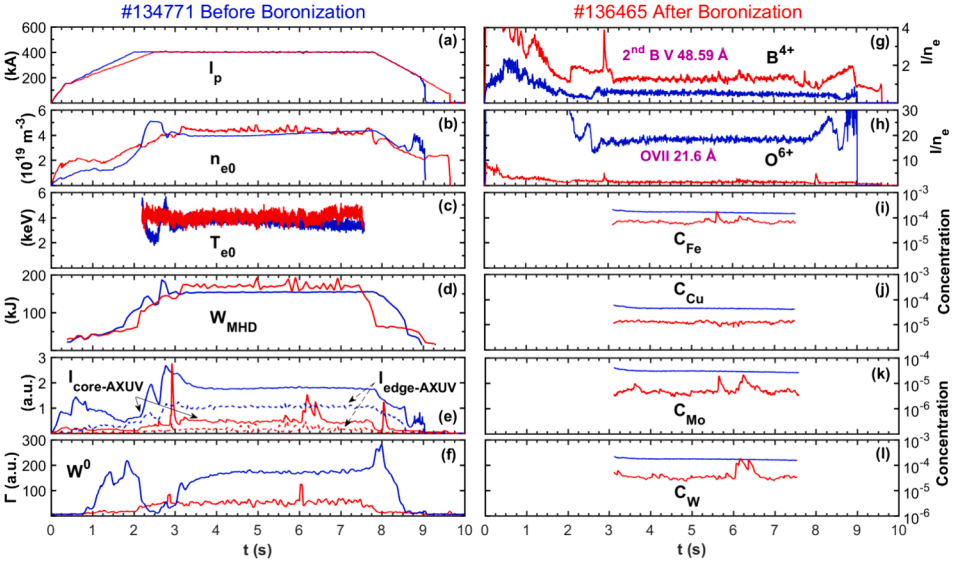

Fig. 2. Time evolution of (a) plasma current, I_p, (b) line-averaged electron density, n_{e0}, (c) central electron temperature, T_{e0}, (d) plasma stored energy, W_{MHD}, (e) line integrated radiation power along central chord, $I_{core\text{-}AXUV}$ (solid line) and edge chord, $I_{edge\text{-}AXUV}$ (dash line), (f) relative flux of tungsten atoms, the n_e-normalized line emission intensity from (g) B^{4+} ions, (h) O^{6+} ions, concentration of (i) iron, C_{Fe}, (j) copper, C_{Cu}, (k) molybdenum, C_{Mo}, (l) tungsten, C_W, before (blue) and after (red) boronization. Same heating power of RF wave is injected in both discharges: P_{ECRH}=3.0 MW, P_{LHW}=1.0 MW. (For interpretation of the references to color in this figure legend, the reader is referred to the web version of this article.)

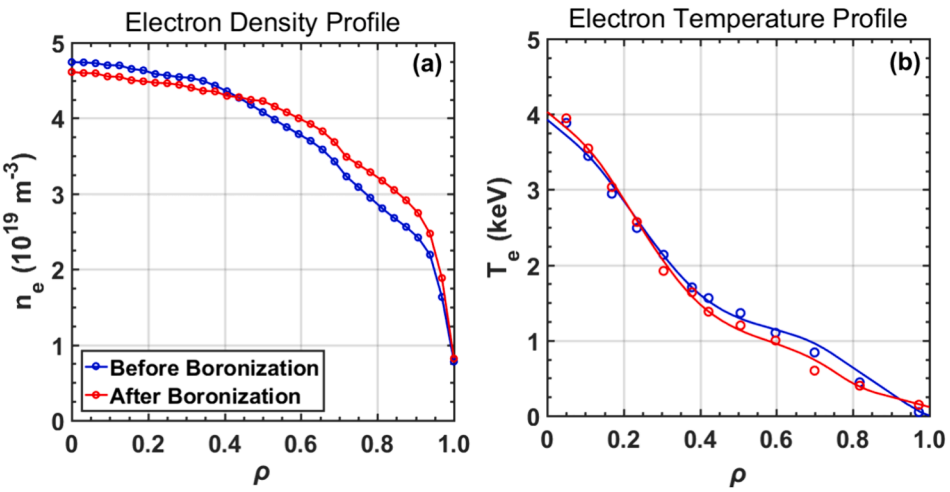

Fig. 3. Radial profiles of (a) electron density, n_e provided by the polarimeter interferometer system and (b) electron temperature, T_e, measured with the heterodyne radiometer system in the shots #134771 (blue) and #136465 (red) at t = 5.0 s, respectively. (For interpretation of the references to color in this figure legend, the reader is referred to the web version of this article.)

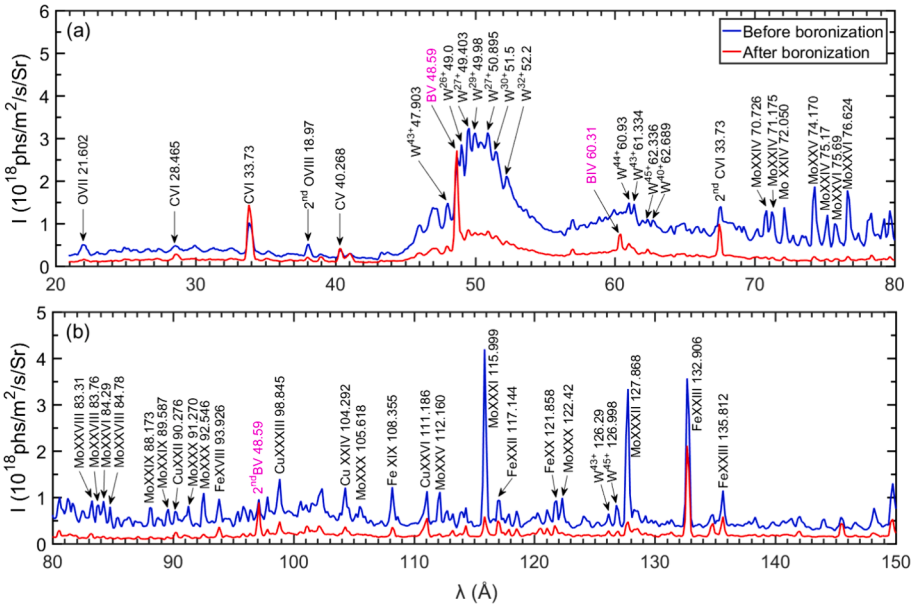

Fig. 4. Comparison of typical EUV spectra at (a) 21–80 Å and (b) 80–150 Å measured by the fast-time-response EUV spectrometer before (blue) and after (red) boronization in the H-mode plasma with similar experimental conditions and plasma parameters: I_p = 400 kA, n_{e0} ~ 4.0 × 10^{19} m^{-3}, T_{e0} ~ 4.0 keV, P_{ECRH} / P_{LHW}=3.0/1.0 MW. (For interpretation of the references to color in this figure legend, the reader is referred to the web version of this article.)

metal impurities, while it is more efficient for tungsten and molybdenum than for iron and copper, which is consist with the results in Fig. 2 (i-l). After boronization, line emissions from B^{4+} (B V at 48.59 Å) and B^{3+} ions (B IV at 60.31 Å) in the spectra with peak distinct from the W-UTA appear in the spectra. Under these plasma conditions, B^{4+} (E_i = 340.2 eV) and B^{3+} (E_i = 259.4 eV) ions are roughly located at ρ ~ 0.75–0.85. In order to avoid a large uncertainty in calculation of line intensity of B V at 48.59 Å, the 2nd order of B V at 48.59 Å isolated from W-UTA with relatively strong intensity is used to study the time evolution of boron ion behaviour in plasma.

3.2. Evolution of boron content after boronization

Time evolution of line emission intensity of 2nd order B V (B^{4+} at 48.59 Å) with shot number is illustrated in Fig. 5. The timing during I_p flat-top phase with stable plasma parameters are chosen for line intensity calculation in each shot. The '1st day', '2nd day', '3rd day' and '4th day' means the first, second, third and fourth day after boronization, respectively. Normally, the boronization is performed at the night before the '1st day'. The 2nd order of B V line is used because the line of B V at 48.59 Å is easily to overlap with W-UTA at ~ 50 Å as shown in Fig. 4 (a). Between #134500 − #137000 shots, five times boronization are performed in EAST. As the discharges progressed, the line emission intensity of 2nd order B V in the plasma gradually diminished. Based on the statistical result, the persistence time of boron in plasma after onetime boronization with 10 g carborane is found to be ~ 2000 s of discharge duration (~150 full discharges). On the third and fourth day after boronization, the boron content in plasma returns to a level before boronization, indicating a complete exhaust of boron in plasma.

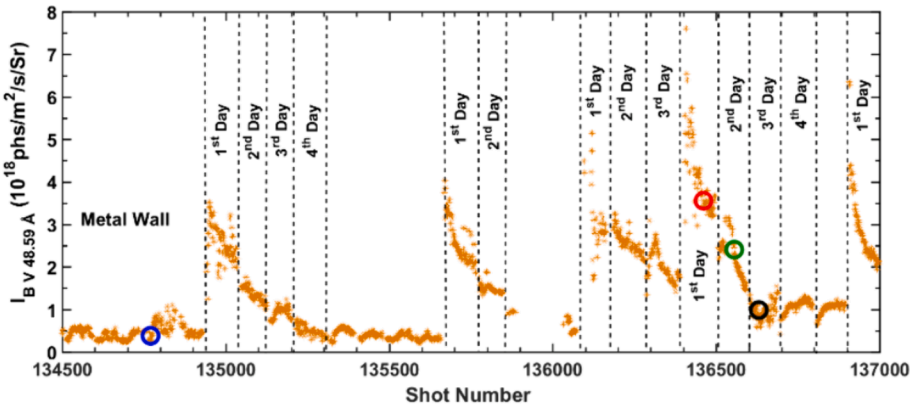

Fig. 5. The evolution of line emission intensity of 2nd order B V (B^{4+}) at 48.59 Å as a function of shot number. The '1st day', '2nd day', '3rd day' and '4th day' represents the first, second, third and fourth day after boronization, respectively. Open circles with different color indicate the four discharges selected in Fig. 8.

3.3. Evolution of metal impurity concentration with boron content

Fig. 6 shows the radiation power loss in plasma core and edge changes with boron content after boronization. These data are collected from I_p flat-top phase in RF heated (ECRH+LHW) H-mode discharges with similar experimental conditions and plasma parameters, e.g., I_p = 400 kA, $n_e \sim 4.0 \times 10^{19}$ m^{-3} and $T_{e0} \sim 4$ keV. The statistical results of radiation from the plasma core and edge indicate that boronization can effectively reduce radiation levels by controlling impurity sources. However, the suppression effect of boronization on various types of metal impurities exhibits certain differences.

The concentration of tungsten, molybdenum, iron, copper in plasma core changes with the boron content are statistically analyzed, the results are illustrated in Fig. 7. Before boronization, the average tungsten concentration, $C_W \sim 2.0 \times 10^{-4}$, almost reaches the threshold level leading H-L back transition under lithium-coated wall condition [36]. After boronization, the C_W in the plasma core decreased by ~ 80 %, to approximately 4.1×10^{-5}. The C_{Mo} dropped by 90 % (from 4.6×10^{-5} to 6.3×10^{-6}), while the C_{Cu} and C_{Fe} decreased by 65 % (from 4.3×10^{-5} to 2.1×10^{-5}) and 50 % (from 2.0×10^{-4} to 6.9×10^{-5}), respectively. On the 3rd day after boronization, the C_{Cu} of 3.5×10^{-5} and C_{Fe} of 1.5×10^{-4} in the plasma approaches those of the uncoated metal wall condition, whereas the C_W of 8.8×10^{-5} and C_{Mo} of 2.0×10^{-5} remain conspicuously below the levels of the uncoated wall. This implies that the high-Z impurity control effect of boronization is more efficient for tungsten and molybdenum compared with iron and copper.

Molybdenum and tungsten primarily originate from the first wall and divertor, which are the main PFCs, hence most of the carborane deposits there. On the other hand, iron and copper mainly come from the antennas of the heating systems and some metal components at LFS (low field side), therefore there may be less carborane deposited on the surface of these parts. As time goes on, the effect of boronization diminishes, and the content of metallic impurities gradually increases.

3.4. Evolution of tungsten impurity profile with boron content

The vertical profiles of line intensity from W^{26+}, W^{27+}, W^{29+}, W^{30+}, W^{32+} and W^{43+} before and after boronization are illustrated in Fig. 8. These four discharges are chosen with similar plasma conditions, the radial profiles of electron temperature and density also resembles that in Fig. 3. The line emission intensity profiles of tungsten ions in the higher charge states are more peaked compared to those in lower charge states. Furthermore, the peak position of tungsten profile does not change significantly under varying wall conditions, as shown in normalized intensity profile Fig. 9. The profile of W^{32+} and W^{43+} are not presented in Fig. 9 due to low signal-to-noise ratio. After boronization, the overall decrease in tungsten content, accompanied by an unchanged profile shape, suggests that the boron coating on the surface of PFCs effectively suppress the source of tungsten impurities without affecting the impurity transport significantly.

4. Summary and discussion

Based on the measurement with impurity spectroscopy at EUV range, the time evolution of the boron content after boronization and the impact of different wall conditions on high-Z metallic impurity behavior in RF heated H-mode discharges are quantitatively studied. The experimental results suggest that after one-time boronization with 10 g of carborane ($C_2B_{10}H_{12}$) the persistence time of boron in plasma is about 2000 s discharge duration (~150 shots). During this period, the content of metallic impurities in plasma core will increase gradually as the boron content decreases. It is found that under uncoated metal wall condition

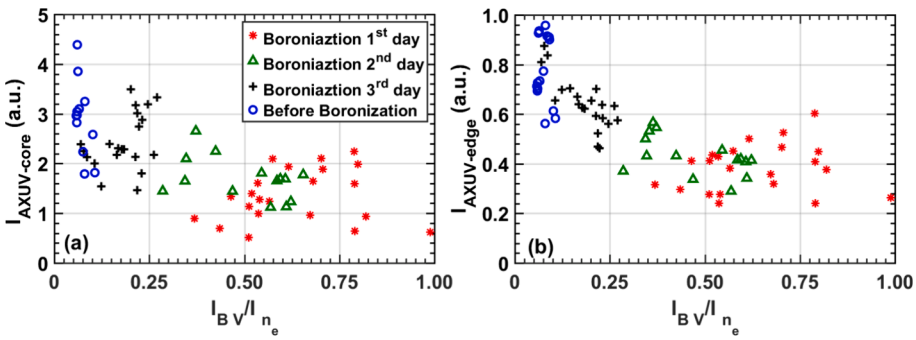

Fig. 6. Radiation power loss in plasma core (a) and edge (b) changes with boron content before and after boronization. (before boronization: blue circles, 1st day: red stars,2nd day: green triangles, 3rd day: black crosses). (For interpretation of the references to color in this figure legend, the reader is referred to the web version of this article.)

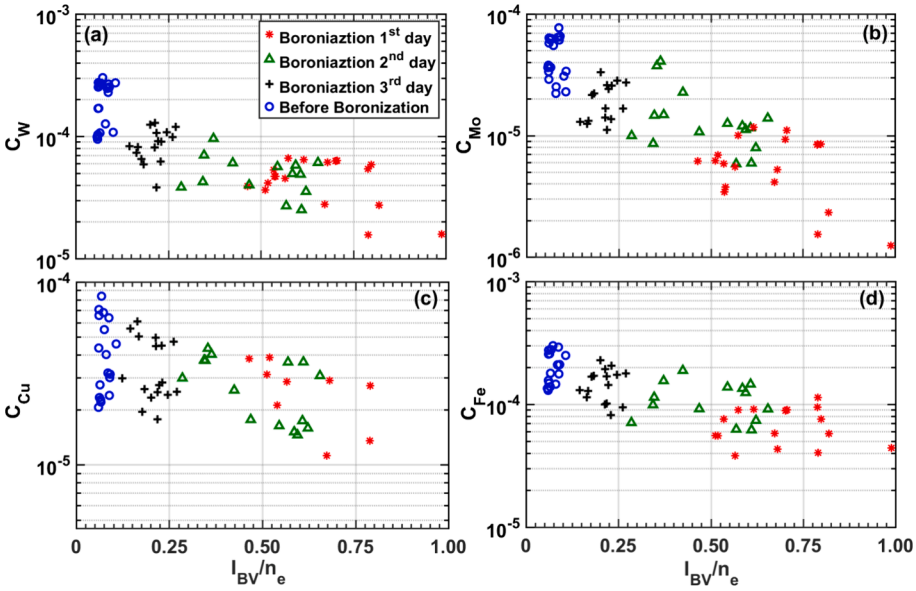

Fig. 7. Impurity concentration of (a) tungsten (C_W), (b) molybdenum (C_{Mo}), (c) copper (C_{Cu}) and (d) iron (C_{Fe}) in core plasma changes with boron content before and after boronization. (before boronization: blue circles, 1st day: red stars,2nd day: green triangles, 3rd day: black crosses). These data are collected from RF heated H-mode plasma with similar experimental conditions and plasma parameters: I_p = 400 kA, $n_{e0} \sim 4.0 \times 10^{19}$ m^{-3}, $T_{e0} \sim 4.0$ keV, P_{ECRH}/P_{LHW}=3.0/(0–1.5) MW. (For interpretation of the references to color in this figure legend, the reader is referred to the web version of this article.)

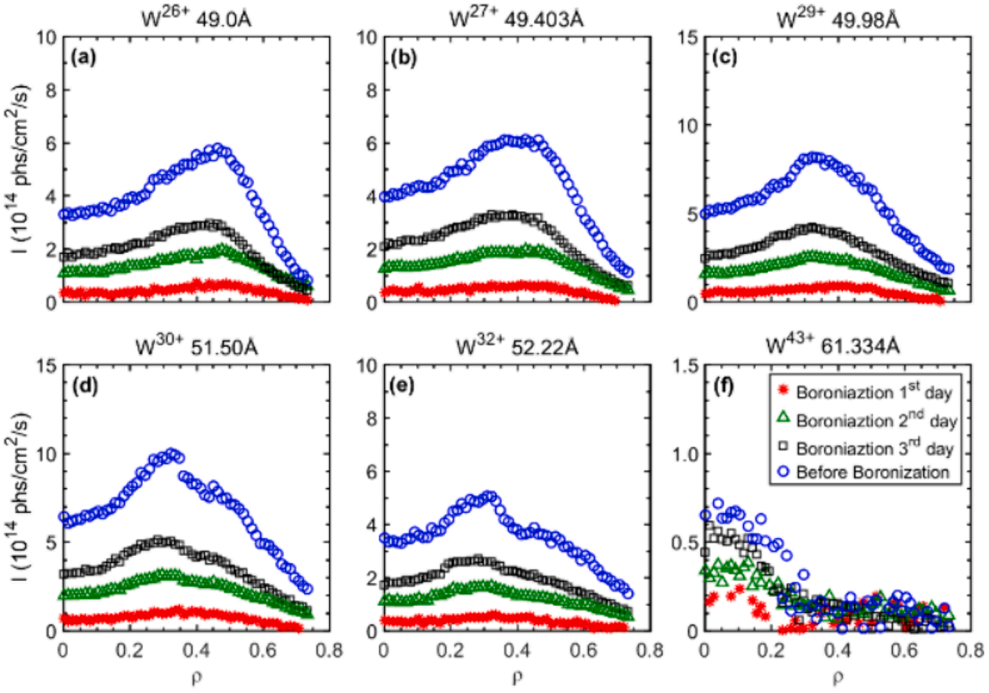

Fig. 8. Vertical profile of line intensity of (a) W^{26+} at 49.0 Å, (b) W^{27+} at 49.403 Å, (c) W^{29+} at 49.98 Å, (d) W^{30+} at 51.457 Å, (e) W^{32+} at 52.22 Å, (f) W^{43+} at 61.334 Å observed in RF wave heated H-mode plasma before boronization (blue circles) and on the first (red stars), second (green triangles) and third day (black squares) after boronization. Discharges are chosen with similar experimental conditions and plasma parameters: I_p = 400 kA, $n_{e0} \sim 4.0 \times 10^{19}$ m^{-3}, $T_{e0} \sim 4.0$ keV, P_{ECRH} / P_{LHW}=3.0/1.0 MW. These four discharges are indicated in Fig. 5 with the open circles in different color. (For interpretation of the references to color in this figure legend, the reader is referred to the web version of this article.)

with RF heated H-mode plasma, the tungsten concentration is about 2.0 $\times 10^{-4}$, which has already reached the threshold concentration leading H-L back transition under lithium-coated wall condition. After boronization, the C_W and C_{Mo} decreased from 2.0 $\times 10^{-4}$ to 4.1 $\times 10^{-5}$ and from 4.6 $\times 10^{-5}$ to 6.3 $\times 10^{-6}$, respectively, showing a reduction of approximately 85 %. The C_{Cu} and C_{Fe} decreased by approximately 50 % and 65 %, respectively, from 4.3 $\times 10^{-5}$ to 2.1 $\times 10^{-5}$ and from 2.0 $\times 10^{-4}$ to 6.9 $\times 10^{-5}$. It would be noted that molybdenum and tungsten primarily come from the first wall and the divertor, where the smooth surfaces allow carborane to be well deposited. Conversely, iron and copper mainly come from the antennas of heating systems and some diagnostic components, where the uneven surfaces do not allow effective deposition of carborane. Moreover, the LHW and ECRH antennas, made of copper, is located at a considerable distance from both the port of the

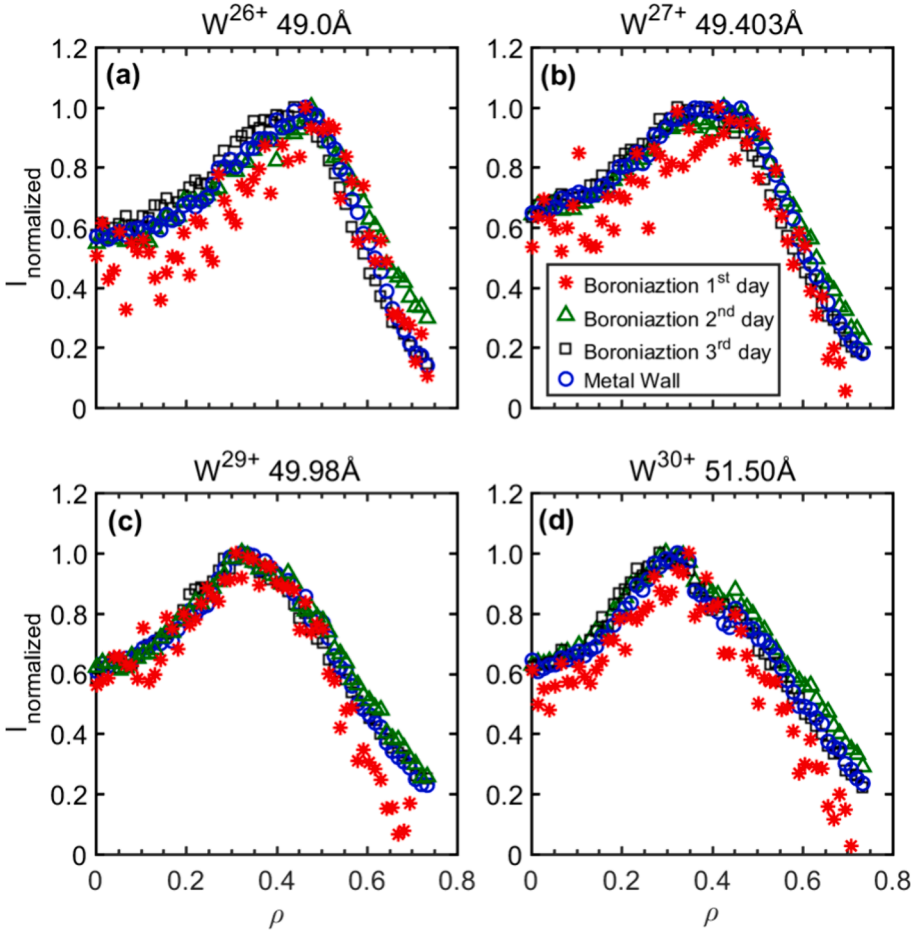

Fig. 9. Normalized intensity profile of (a) W^{26+} at 49.0 Å, (b) W^{27+} at 49.403 Å, (c) W^{29+} at 49.98 Å, (d) W^{30+} at 51.457 Å under different wall conditions, calculated based on the data from Fig. 8.

ICRF antenna and the oven which used for evaporate carborane. Consequently, only a small amount of carborane is deposited on the LHW and ECRH antennas after ICRF-assisted boronization. This may be the reason why the effect of boronization on suppressing iron and copper impurities is slightly weaker than that on molybdenum and tungsten. A comparison of tungsten profiles before and after boronization revealed that boronization led to an overall reduction in the spatial distribution of tungsten ions, without an obvious change in the profile shape of the tungsten ions distribution. This indicates that boronization can effectively reduce the source of metallic impurities without affecting the impurity transport significantly. This work not only offers a new perspective on understanding the mechanisms of high-Z metallic impurity control, but also provides important guidance for the selection of materials for PFCs and wall conditioning.

The materials used in boronization, carborane ($C_2B_{10}H_{12}$), contain a large amount of hydrogen, resulting in a high H/(H+D) ratio of 45 % in the plasma. Reducing the H/(H+D) ratio to below 10 % requires around 1000 s of discharge duration, after which ICRF can be injected into plasma with better coupling efficiency. Therefore, improvements in boronization techniques are necessary to achieve a lower H/(H+D) ratio. In addition, two multifunctional visible spectrometers working at wavelength range of 300–800 nm have been newly developed in EAST to survey edge impurity source and their distribution, such as W^0, W^+, Mo^0, B^+, C^{2+}. Spectral lines from B^+ could be utilized to evaluate the boron coating condition and also boron coating lifetime which is expected to be much shorter than the boron persistence period in plasma. Currently the system commissioning is been carried out involving wavelength calibration, absolute intensity calibration, line identification of visible spectra. Combination of the measurement from visible spectrometers and the EUV spectrometers will allow a quantitative analysis on the impurity sputtering, influx and density distribution, and therefore make it capable of study on impurity production and transport through plasma edge into core region for multiple low-Z and high-Z impurity species.

CRediT authorship contribution statement

Yunxin Cheng: Writing – review & editing, Writing – original draft, Investigation, Formal analysis, Data curation. **Ling Zhang:** Writing – review & editing, Supervision, Project administration, Investigation, Formal analysis. **Ailan Hu:** Investigation, Formal analysis, Data curation. **Shigeru Morita:** Methodology, Investigation. **Wenmin Zhang:** Investigation, Data curation. **Chengxi Zhou:** Investigation, Data curation. **Darío Mitnik:** Data curation. **Fengling Zhang:** Investigation, Data curation. **Jiuyang Ma:** Investigation, Data curation. **Zhengwei Li:** Visualization, Software. **Yiming Cao:** Investigation, Data curation. **Haiqing Liu:** Validation, Supervision, Project administration.

Declaration of competing interest

The authors declare that they have no known competing financial interests or personal relationships that could have appeared to influence the work reported in this paper.

Data availability

Data will be made available on request.

Acknowledgements

This work was supported by the National MCF Energy R&D Program (Grant No. 2022YFE03180400, 2022YFE03020004), National Natural Science Foundation of China (Grant No. 12322512), and Chinese Academy of Sciences President's International Fellowship Initiative (PIFI) (Grant Nos. 2024PVA0074, 2025PVA0060).

References

[1] Y. Wan, et al., Nucl. Fusion 57 (2017) 102009.
[2] C. Xuan, et al., Nuclear Materials and Energy 34 (2023) 101377.
[3] Y. Song, et al., IEEE Trans. Plasma Sci. 50 (2022) 4330.
[4] J. Huang, et al., Phys. Plasmas 30 (2023) 062504.
[5] R. Neu, et al., Plasma Phys. Controlled Fusion 49 (2007) B59.
[6] J. Bucalossi, et al., Fusion Eng. Des. 89 (2014) 907.
[7] G. Matthews, et al., Phys. Scr. T145 (2011) 014001.
[8] G. Zuo, et al., Plasma Physics and Control Fusion 54 (2012) 015014.
[9] S. Hong, et al., J. Nucl. Mater. 415 (2011) S1050–S1053.
[10] Y. Yamauchi, et al., Fusion Eng. Des. 81 (2006) 315–319.
[11] Z. Wang, et al., Plasma Sci. Technol 3 (2001) 1063.
[12] M. Apicella, et al., Nucl. Fusion 45 (2005) 685–693.
[13] H. Wang, et al., J. Phys. Conf. Ser. 100 (2008) 062011.
[14] A. Loarte, et al., ITER Technical Reports, (2024) ITR-24-004.
[15] L. Zhang, et al., Nuclear Inststrument and Methods in Physics Research A 916 (2019) 169–178.
[16] L. Zhang, et al., Rev. Sci. Instrum. 86 (2015) 123509.
[17] Z. Xu, et al., Nuclear Instrument and Methods in Physics Research A 1010 (2021) 165545.
[18] Y. Cheng, et al., Rev. Sci. Instrum. 93 (2022) 123501.
[19] Y. Cheng, et al., Nuclear Inst. and Methods in Physics Research, A (2023, 1057,) 168714.
[20] G. Zuo, et al., J. Nucl. Mater. 438 (2013) S90–S95.
[21] Z. Sun, et al., Nuclear Materials and Energy 19 (2019) 124–130.
[22] Z. Sun, et al., Fusion Eng. Des. 89 (2014) 2886–2893.
[23] Y. Guan, et al., Nuclear Materials and Energy 34 (2023) 101368.
[24] J. Li, et al., Nucl. Fusion 39 (1999) 973.
[25] X. Gao, et al., J. Nucl. Mater. 390–391 (2009) 864–868.
[26] J.S. Hu, et al., Fusion Eng. Des. 84 (2009) 2167–2173.
[27] Y. Cheng, et al., IEEE Trans. Plasma Sci. 50 (2022) 691–699.
[28] H. Zhao, et al., Rev. Sci. Instrum. 89 (2018) 10H111.
[29] J. Li, et al., J. Instrum. 15 (2019) C02048.
[30] H. Liu, et al., Rev. Sci. Instrum. 87 (2016) 11D903.
[31] Y. Duan, et al., Plasma Sci. Technol 13 (2011) 546.
[32] K. Behringer, et al., Plasma Phys. Controlled Fusion 31 (1989) 2059.
[33] H. Mao, et al., Rev. Sci. Instrum. 88 (2017) 043502.
[34] L. Li, et al., Plasma Sci. Technol 23 (2021) 075102.
[35] W. Zhang, et al., Phys. Scr. 97 (2022) 045604.
[36] L. Zhang, et al., Nuclear Materials and Energy 12 (2017) 774–778.